A fiber Fabry-Perot cavity for photothermal gas detection

Jana Blechmann

Bachelorarbeit in Physik angefertigt im

Physikalischen Institut

vorgelegt der Mathematisch-Naturwissenschaftlichen Fakultät

der

Rheinischen Friedrich-Wilhelms-Universität Bonn

August 2024

Ich versichere, dass ich diese Arbeit selbstständig verfasst und keine anderen als die angegebenen Quellen und Hilfsmittel benutzt sowie die Zitate kenntlich gemacht habe.

Bonn, 07.08.2024
Datum

Unterschrift

1. Gutachter: Prof. Dr. Sebastian Hofferberth
2. Gutachter: Prof. Stefan Linden

Acknowledgments

As I was welcomed in such a loving way, I wanted to take the time to thank everybody of the Nonlinear Quantum Optic research group for making me feel like a part of the group.
I further would like to especially thank Dr. Prof. Sebastian Hofferberth and Karol Krezmpek for giving me the opportunity to work on such an interesting project, Prof. Linden for allowing me to use the PPGT2 and agreeing to be second supervisor, Dr. Hannes Pfeifer for helping me at every given moment as well as Lukas Tenbrake, Daniel Stachanow and Florian Griefer of the Fiber Cavity Optomechanic group for guiding and accompanying me through those four months.

Contents

Chapter 1

Introduction

Detecting different gases and their respective concentration plays a crucial role for applications in various fields, such as medicine, environmental research and the industrial sector. One example being the detection of methane gas in mines increasing the safety of mine workers.
With its wide field of applications, the development of gas sensors, which are low in cost, compact, stable, and highly sensitive in detection is major research effort [7].
In gas sensors relying on photothermal spectroscopy (PTS), a pump laser, operating at one of the absorption frequencies of a to-be-tested gas species, excites the gas molecules, increasing the molecules energy. The excited gas molecules then dissipate the additional energy primarily in form of collisions, which leads to an increase in the temperature along the pump laser beam. With changing temperature, the gas molecules redistribute them-self, changing the density in the affected volume. The density shift gives rise to a variation of the refractive index of the gas. Consequently, measuring this variation in the refractive index makes it possible to draw conclusions about the present gas and its concentration.
In refractive index spectroscopy, another laser, namely the probe laser, is utilized for measuring the refractive index. When the probe laser passes through the modulated gas, the phase of the laser light shifts. As the effect is marginal, resolving it poses significant challenges. To enhance the detectability of this effect, a resonator can be incorporated, allowing the light to undergo the phase shift multiple times.
A fiber Fabry-Perot cavity (FFPC) is one realization of such an optical resonator, standing out by its compact design and ease of application. Here, the probe laser can be directly coupled with an optical fiber into the cavity volume, thus avoiding the need of complex free-space optics. For FFPCs, the cavity is formed at the volume between two mirror-mounted fibers. Further integrating a fiber-guiding two-channel ferrule enhances portability, robustness and stabilization and has already been successfully shown by Karol Krzempek et al. in [9]. In order to further miniaturize this detection scheme and stably supply a fiber-coupled pump beam to the cavity volume, an additional channel in the ferrule would be required.
This thesis aims for the manufacturing of a three-channel ferrule using a 3D-printer and building a fiber Fabry-Perot cavity for photothermal gas detection as a cooperation project with Karol

Krzempek from the Wroclaw University of Science and Technology.

The thesis is split into two main sections.
The first section describes the fabrication procedure to 3D-print ferrules that can replace the established glass-based ferrules. Their suitability to realize fiber optic cavities is demonstrated.
The second section presents the process of building the three-channel ferrule for efficient photothermal gas detection.
Characterization and optimization processes are developed and an outlook towards a fully operable three-channel device for photothermal gas detection is given.

Chapter 2

Tunable, passively stabilized fiber Fabry-Perot Cavity

2.1 The Fabry-Perot cavity

In its simplest form, a Fabry-Perot cavity consists of two plane-parallel, partially reflective mirrors positioned at a distance L.

The laser light, coupled into one mirror, gets partially transmitted into the cavity volume. It then gets reflected on the mirrors, leading it to travel back and forth inside the cavity volume. The lights wave characteristics lead to interference of the partially reflective waves of light inside the cavity. A standing wave inside the cavity can be formed under the resonance condition [2]

$$\nu = N\Delta\nu_{\mathrm{FSR}} \tag{2.1}$$

with N being an integer larger than 0. The frequency spacing between resonance frequencies, the **free spectral range**, is given by [2]

$$\Delta\nu_{\mathrm{FSR}} = \frac{c}{2nL} \tag{2.2}$$

with n being the refractive index of the medium inside the cavity and c the vacuum speed of light. If the resonance condition is fulfilled, the total reflected light reaches its minimum value and the frequency dependend reflective signal follows the shape of a Lorentzian curve. The ratio of the on-resonant and the off-resonant reflective signal value is defined as the coupling depth.

The reflectivity of the mirrors is specified by how many parts per million (ppm) of incoming light are estimated to be transmitted.

One can now further enhance the efficiency by not using planar mirrors, but choosing curved mirrors instead. In cavities with curved mirrors, light refocuses by itself, as its circulating in between the mirrors.

To first order, the light inside the cavity follows a Gaussian distribution along the transversal plane.[1]

2.1.1 The fiber Fabry-Perot cavity

Aiming to build a Fabry-Perot cavity used for photothermal gas detection, a compact, light-weight and monolithic realization of an optical cavity is needed.
Fiber Fabry-Perot cavities fulfill these requirements. Using a high-power CO_2 laser operating at the absorption peak of the fiber material (silica), it is possible to 'shoot' a spherically formed depression onto cleaved fiber tips. The fiber tips can then be coated with alternating dielectric layers, thus creating a spherical Bragg mirror. The input beam can be directly coupled into the space in-between two coated fiber tips by simply coupling the laser light into one of the fibers.
The fiber depressions used in this work are prepared at the Forschungs- und Technologiezentrum Detektorphysik (FTD) shooting setup of the University of Bonn. Coating the shot fiber tips with dielectric layers was done by the company LAYERTEC [13].
A thorough explanation on the principles of cavities, specifically fiber Fabry-Perot cavities and fiber mirror fabrication, can be found in [5], [6] or [4].

2.1.2 The hybrid Fabry-Perot cavity

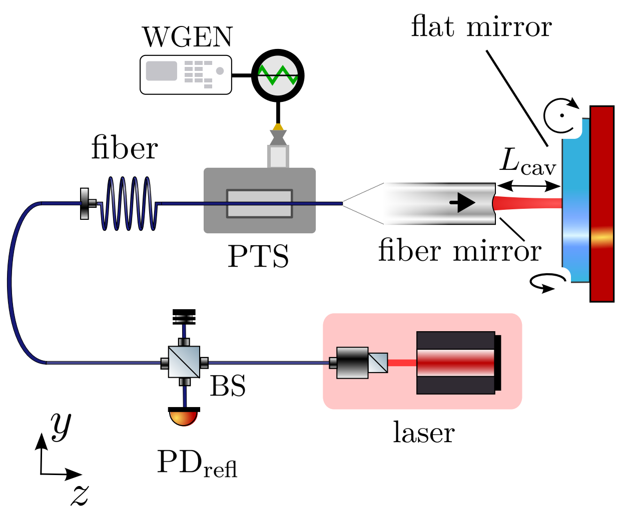

Figure 2.1: Setup of a hybrid Fabry-Perot cavity: A 1550 nm laser is coupled directly into a fiber, which then passes through a beam splitter (BS), splitting into an open end, a photo diode (PD) measuring the reflected signal and the fiber mirror. The fiber is positioned onto a piezo stage (PTS) coupled to a frequency generator (WGEN) with a triangular shaped signal output. A close-up of the fiber mirror facing the planar mirror can be seen in the upper right corner.

[1] This also is known as the fundamental transversal mode, TEM_{00}. For further information on the light distribution see [2]

As it is quite challenging to fabricate perfectly formed spherical depressions exactly on the center of a fiber tip, each fiber mirror still has to be tested in their coupling depth before application. For that purpose, a specific setup is being used, where a fiber mirror is not directly aligned onto another fiber, but instead onto a planar mirror. This creates a hemispherical cavity known as a **hybrid Fabry-Perot cavity**. The fiber, secured on a fiber holder, is placed on a piezo-driven stage. This enables continuous variation of the distance between the fiber and the planar mirror, up to micrometers. The setup is depicted in Figure 2.1. For finding fiber tips with high coupling depth, one usually positions the fiber tip as close to the mirror as possible. This is not visible by eye, so that a 200x microscope camera is positioned in a roughly 45° angle to the mirror surface. The fiber and its reflection on the mirror should be, now enlarged, visible. an example image is shown in Figure 2.2

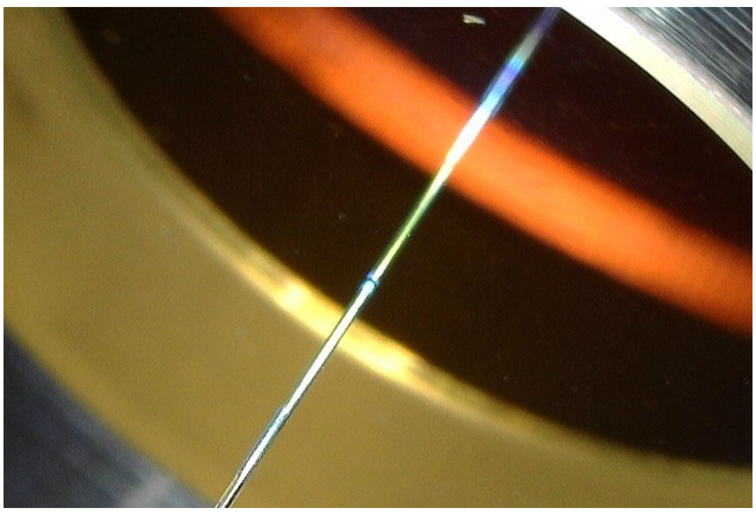

Figure 2.2: Microscope image of a fiber and its reflection on a planar mirror.

The reflection signal is observed on an oscilloscope, which is connected to the photo diode, see Figure 2.1. One now adjusts the alignment between fiber and planar mirror by tilting the plane mirror until a resonance peak is being detected.
More often than not, a fiber has not been shot, but still was coated. One has to keep in mind that the production process of these fiber mirrors is challenging, leading to inconsistencies in achieved coupling depths of the fiber mirrors.

Measuring the coupling depth with hybrid Fabry-Perot cavity

For the purpose of photothermal gas detection, infrared 1550 nm light is required. Thus, also a 1550 nm single mode fiber is needed to guide the IR light. Achieving a coupling depth of over 20% can be seen as sufficient enough for the intended usage here.
This specific shooting run of the 1550 nm fibers unfortunately yielded a very high failure rate. Thus, different methods to sort out unusable fibers were adopted prior to building a hybrid Fabry-Perot

cavity.

First, the fiber tips were examined with a 500x USB microscope. This gives a first idea on whether the tip has been shot properly. This way fiber mirrors which most likely would not show any resonances can be ruled out in advance. Shot fiber tips, see Figure 2.3a, feature a curved surface, while non-shot fiber tips, see Figure 2.3b, feature a planar surface.

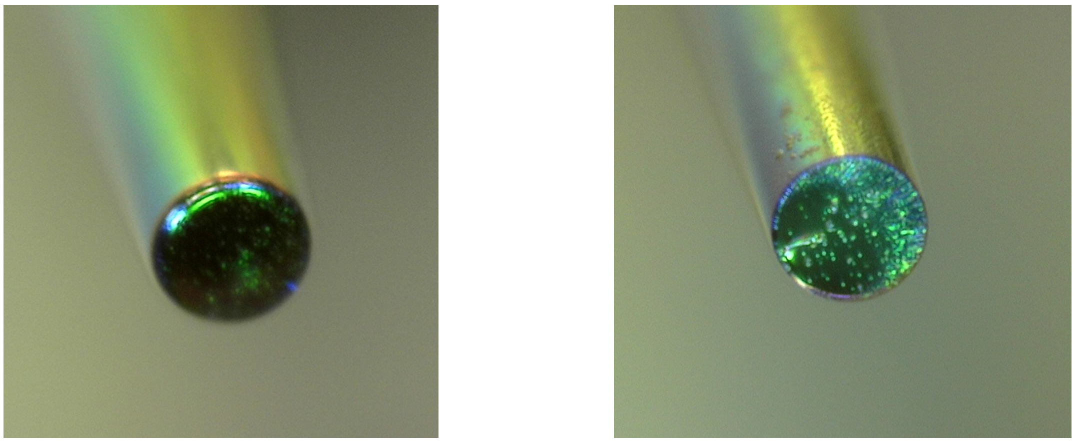

(a) Close-up of fiber tip, which has been shot. One can see the slight reflection of a curved surface.

(b) Close-up of fiber tip, which has not been shot. The surface reflection indicates a planar surface.

Figure 2.3: Fiber tip images taken with 500x USB-microscope camera.

Additionally, every selected fiber was cleaned. At first, this was done by applying distilled water on the fiber mirrors with a pipette and blowing it off with a nitrogen gun afterwards.

However, comparing the fiber mirrors with the USB microscope camera before and after that cleaning process showed no significant difference.

Hence, a more aggressive method was employed. Here, the fiber mirrors were swiped with a lens cleaning tissue and distilled water, which got rid of most of the dirt. Applying too much force while swiping can lead to the fiber tips breaking off.

Subsequently, the fibers are to be installed into the resonance measuring setup. After the fiber mirror is positioned at about 1 mm distance to the planar mirror, the alignment should be adjusted in a way that the fiber itself and its reflection on the mirror form one straight line. An example is depicted in Figure 2.2. The fiber mirror then can be moved closer to the planar mirror so that the spacing in-between is barely visible when viewed with a 200x microscope. This simplifies the alignment procedure.

Two of the tested 1550 nm fiber mirrors were characterized as sufficient for the final application with one reaching a coupling depth of roughly 60% and the other of 30%. Both fibers and the planar mirror have a transmission of 150 ppm, leading to optimal impedance matching and therefore, in theory, optimal coupling depth[2].

[2]For further information, see [5] or [6].

2.2 Printing a ferrule

As bare fibers typically hold a diameter of 0.125(5) mm and coating adds 0.01 mm at most, aligning the fiber tips in free space to create a cavity turns out to be tedious.
Using a ferrule to help in guiding the coated fibers to the properly aligned position has already been shown in previous research [4]. The ferrules used so far are made out of glass and are available on the market[3]. These are 8.00(5) mm in length, 1.225(25) mm in width and height and feature a 0.131(2) mm diameter channel. The channel is positioned in 0.875(25) mm height proceeding along the length and is centrally arranged in respect to the width.
However, as the desired ferrule should be customized with new features, the primed glass ferrules would be complicated to use. This led to the thought of producing a ferrule from scratch. One way would be printing ferrules directly with a 3D printer capable of precision below micrometer scale.
Specifically for photothermal gas detection, a third fiber needs to be positioned transversely into the cavity volume, on the same level as to two cavity fibers. This fiber will serve as the pump light source, which will be used to excite the gas molecules in the final realization. Thus, the objective is to 3D-print a prototype of a three-channel ferrule in order to ease the process of alignment. For that, the first aim was to successfully print a functioning two-channel ferrule before moving on to a three-channel ferrule.

The 3D printer used for this purpose is called the Photonic Professional GT2 (PPGT2), manufactured by the company Nanoscribe GmbH & Co. KG [17].
The process of 3D printing typically can be split up into four main steps.
First, the object, which is supposed to be printed, needs to be modelled. For the used PPGT2 3D printer, this can be done using the 3D-CAD-Software Autodesk Inventor [16]. Autodesk Inventor includes modelling tools such as visual representation of the designed model, which drastically simplifies 3D modelling.
Second, the exported file then needs to be imported into the print job developing software DeScribe [12], which is specifically for the on-site used Nanoscribe PPGT2. In DeScribe, the model is converted into laser trajectories. The writing parameters, manually adjustable in DeScribe, determine the trajectory properties, such as speed, degree and location of polymerization and more.
Third, the printing job file for the set trajectories with chosen writing parameters is then imported into the interface NanoWrite [17], where the instructions are transferred on to the PPGT2 and executed and printed.
The fourth step is then the developing, rinsing and curing steps post-printing.
In the subsequent section, a detailed description of the two-channel ferrule printing process is given.

[3]The glass ferrules were Vitrocom - Q6606, which are not available anymore. Proportions were taken from an old screenshot of the measurements, not publicly available.

2.2.1 Designing a two-channel ferrule

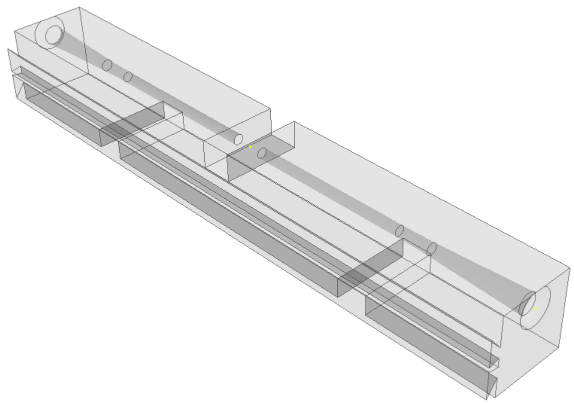

Figure 2.4: Autodesk Inventor design of the first ferrule with $l = 8\,\text{mm}$, $h = 1\,\text{mm}$, $w = 1\,\text{mm}$, the diameter of the channel $d = 0.130\,\text{mm}$ and its position at $h_c = 0.8\,\text{mm}$, $w_c = 0.5\,\text{mm}$. The design features additional feet and grooves for the cavity volume and for cut-ins.

Inspired by the design of the already successfully used glass ferrules, dimensions of length, height and width were set to $l = 8\,\text{mm}$, $h = 1\,\text{mm}$ and $w = 1\,\text{mm}$. The diameter of the channel was chosen as $d = 0.130\,\text{mm}$ and the position of its core at $h_c = 0.8\,\text{mm}$, $w_c = 0.5\,\text{mm}$. For easy insertion of the fibers, a cone-shaped entrance was added. The ferrule also should be removable from the substrate, on which it is printed on. Thus, triangle-shaped feet were added, which should help in breaking the ferrule off of the substrate. Two grooves on the bottom side of the ferrule were also included, as further discussed in section 2.3. The design is depicted in Figure 2.4. Over various printing runs, the design has been steadily updated to fit the parameters of the employed PPGT2 Nanoscribe 3D printer.

2.2.2 Printing parameters

Typically, 3D printers operate by applying energy in form of UV-light onto a liquid resin, which provokes polymerization and hardening of the resin. For the PPGT2, the underlying process is the free radical polymerization[4]. Applying energy in form of focused laser light, one can reduce the size of the area, which undergoes polymerization.
The resin is applied to an ITO-covered substrate[5]. This makes it possible to locate the interface between the substrate and resin and thus, defining the starting plane of the printing procedure.

[4]In Free Radical Polymerization an initiators bond is split under energy application, which then creates free radicals. These radicals then form polymer chains with monomers, a detailed explanation can be found in [10].

[5]ITO stands for Indium tin oxide and is the material, with which one side of a glass substrate is thinly covered. The material shows a larger difference in the reflective index than glass compared to the resin [20].

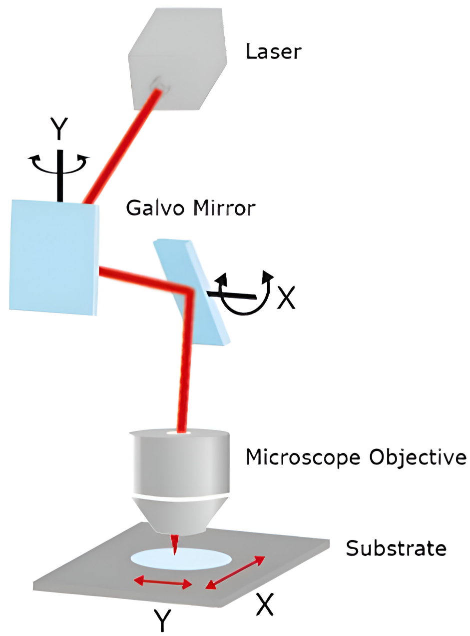

Figure 2.5: Sketch of the PPGT2 setup: The laser is focused onto two tiltable mirrors, the galvo mirrors, guiding the laser into the microscope objective and further into the resin. The resin is applied to a substrate, that can be moved by a translation stage [20].

The PPGT2 is capable of only polymerizing resin in a small area close to the laser focus, by making use of **Two Photon Polymerization**. Here, laser light of double the wavelength (IR) as UV-light is used. Consequentially, two photons instead of one are needed to enable the same polymerization process. This is a non-linear process, which requires high intensity laser light. This is only possible at the laser lights focus, reducing the polymerized area to a spheroidal, controllable voxel shape [8].
The basic composition of the PPGT2 set up is depicted in Figure 2.5. The PPGT2 additionally features different printing settings, which further described in [21]. With the set dimensions of the designed ferrule, the voxel size given by the 25x objective is sufficient enough in accuracy.

Printing mode

There are two printing modes, piezo and galvo, that offer two different ways of printing voxels. With the piezo mode, the laser beam out of the objective is stationary and perpendicular to the substrate. The relative position of the laser beam to the substrate is adjusted through movement of the substrate by the piezo stage, enabling an accuracy of 10 nm. Thus, high printing precision and minimal voxel size can be achieved with the piezo mode.
In the galvo mode, in addition to using the movement of a coarser translation stage, also tilting of the galvo mirrors, compare with Figure 2.5, is executed. Tilting of the mirrors varies the angle of the deflection of the laser beam onto the objective lens, thus also tilting the outgoing laser beam. The tilted beam, in comparison to the undeflected beam, is visualized in Figure 2.6a. However with

increasing deflection angle, stronger optical aberrations occur. With larger angles, distance to the substrate increases, leading to attenuation of the beam intensity and additional distortion effects become more pronounced. The galvo mode enables higher printing speed and larger range of the printing area.

Block splitting

Splitting the print into blocks, one can combine the galvo mode with the translation stage movement to decrease printing time while suppressing distortion effects. With the stage, movement in between blocks is regulated. The individual blocks are then printed in galvo mode. Thus, the smaller the block size, the smaller the beam distance between objective and printing location, which leads to reduced aberration effects.

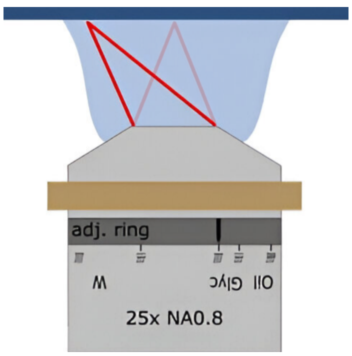

(a) Piezo mode laser path in light-red and galvo mode tilted laser path in red galvo . With changeable tilt angle, the area covered without stage movement is visibly larger in galvo mode.

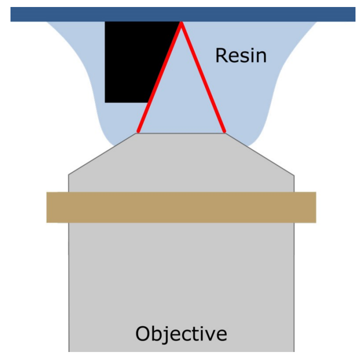

(b) Laser path with block printing, depicting the needed shear angle.

Figure 2.6: Sketch of different laser trajectories out of the objective onto the substrate[20]

Additionally, by choosing the Shell and Scaffold mode the printing time is reduced, as only the shell and a supporting scaffold of the individual blocks gets polymerized.
As one can see in Figure 2.6b, the already printed block can cover the laser path to the next to-be-printed block, so that choosing a shear angle for the blocks is mandatory for printing with the galvo mode. This is also known as the shadowing effect [20]. The larger the block size, the larger the shear angle has to be. The edges of the blocks are clearly visible on the printed objects, which can be seen in Figure 2.7a.

Developing and Rinsing

After the printing process, placing the printed object into a developer, here PGMEA[6], enables the removal of the excess liquid resin. Subsequently, the PGMEA then can be removed from the print through rinsing with IPA[7].

[6] Short for Propylene-glycol-methyl-ether-acetate, for more information on the development process, see [3]
[7] Isopropanol

A development time of about 20 minutes and rinsing for 15 minutes is recommended [19].

Finding writing parameters

However, 20 minutes of developing time was not enough to fully flush the undesired resin out of the ferrules channel. After the ferrule has been completely dried, the channels were visibly blocked with polymer. This can be seen in Figure 2.7a. The shadow on the channel indicates, that only the opening area of the channel was successfully flushed. Increasing the developing time up to 1 hour was sufficient enough to fully remove the liquid resin from the channel. The rinsing time with IPA was also increased to 1 hour. The long exposure to PGMEA can lead to stronger shrinking of the polymer after drying [22].
Post development UV curing polymerizes the not yet polymerized resin in between the block scaffold and was applied here. This again can lead to further shrinking. Curing the print while still placed in IPA is supposed to counteract that process. Based on that, curing in IPA has been done for every print.

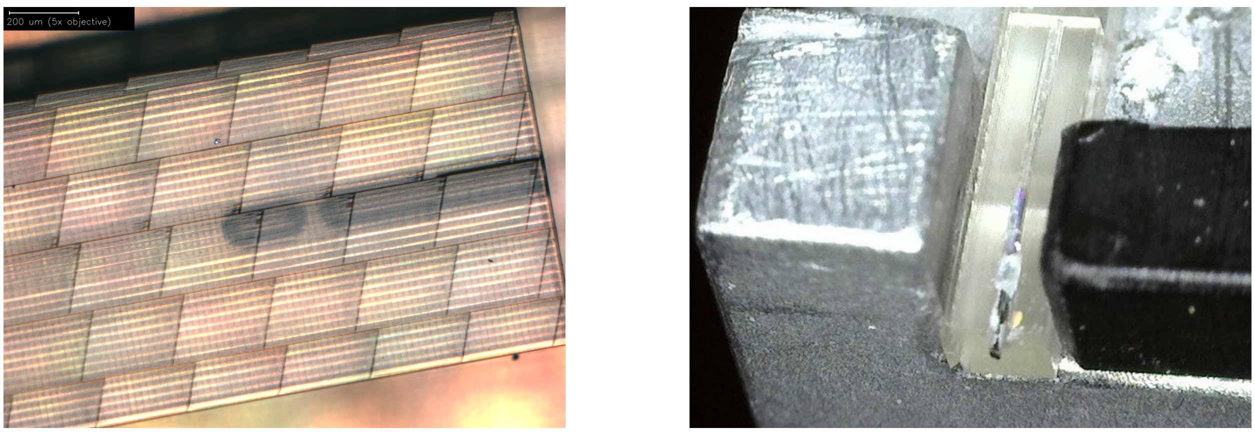

(a) 5x microscope objective image of a ferrule channel opening. The shadow on the channel's path indicates that the channel is partially blocked with polymerized resin.

(b) Microscope image of broken channel opening with stuck fiber.

Figure 2.7: Images of ferrules unfit for usage.

As the ferrule needs to be placed inside PGMEA for 1 hour, the feet on the ferrule proved to be unnecessary, as the print came off the substrate on its own while developing. This did not cause any problems, since the ferrule was simply removable from the liquid PGMEA with a pair of plastic tweezers. For the prints following the first one, the feet were removed from the design.

A block size of 200 µm x 200 µm x 200 µm with a shear angle of 15° was chosen for the first print and was not altered for the following prints.

The printing material can shrink from 2% up to 12% after development [19], thus finding the

right diameter size of the printed ferrule channel was more challenging.
For ensuring passive stability of the cavity, the coated fibers should fit but not be able to move around more than necessary. Bare fibers with a 0.125(5) mm diameter are available in large amounts and were inserted before testing with coated fibers.
The first chosen 0.130 mm channel diameter proved to be too tight for bare fibers to fit, so that the channel was expanded with a 0.08 mm diameter diamond wire [18].
With the bare fiber able to fit, a coated fiber, inapt for utilization, was inserted. The ferrule channel was further broadened until the coated fiber was able to fit inside. For the first ferrule, this resulted in breaking of the channel opening edges, which can be seen in Figure 2.7b. Therefore, the diameter of the channel had to be set larger and closer to the center of the ferrule. The height was altered to $h_c = 0.714$ mm with which, as far as the breaking of outer edges goes, no further problems occurred. A later design of a ferrule with no feet, lower and wider channel and a curved cut-out for the cavity area can be seen in Figure 2.8.

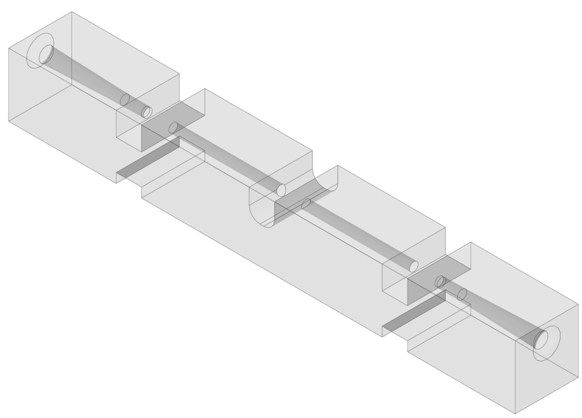

Figure 2.8: Autodesk Inventor design of a ferrule with $l = 8$ mm, $h = 1$ mm, $w = 1$ mm, the diameter of the channel $d = 0.140$ mm and its position at $h_c = 0.714$ mm, $w_c = 0.5$ mm. The design features additional grooves for the cavity volume and for cut-ins.

Although the diameter was increased with every print up to 0.140 mm, each ferrule's channel needed to be broadened additionally. This can be reasoned with the denoted shrinking percentage and chosen size of the ferrule.
With the objective of examining the behaviour of the printed ferrules in a vacuum environment, the ferrules, widened enough for a coated fiber to fit, were placed inside a vacuum chamber. Two ferrules were left inside a vacuum chamber ($\sim 1 \times 10^{-6}$ mbar) for over 24 hours. The ferrules showed no visible alteration and no noticeable shrinkage.

2.3 Tuning of cavity length

Adjusting the cavity length L to fulfill the resonance condition stated in Equation 2.1 demands for detuning on nanometer scale. The use of a piezo element, which enables continuous variation of the length of the cavity, makes it possible to cycle through the resonance positions regularly.

2.3.1 Piezoelectric crystal

Piezoelectric elements applied as an actuator are able to convert electric/thermal energy into mechanical strain. The element's material is classified broadly in the groups of ceramics, crystalline and polymers.
Focusing on the utilized piezo ceramics, these consist of asymmetric electric dipoles, which can change their orientation with the supply of sufficient energy. With an electric field applied, such that the dipoles align their orientation, the material stretches parallel to the direction of the electric field and contracts in others. The volume remains constant. A thorough explanation can be found in [11].
Applying an actuator directly onto the ferrule, makes it possible to apply strain in cavity length direction onto the polymer. The strain should not however provoke breaking of the ferrule. In [19] it is specified, that the printing material is able to elongate up to 5.3% of its original size before breaking.

The piezo ceramics used are 10.00(5) mm long, 1.00(5) mm wide and 1.00(2) mm high [15], fully covering the surface of the ferrule. Additionally, electrodes need to be connected on to the piezo in order to apply an external voltage. For that, silver glue is used, as the material of the glue should be conductive. That is also used for fixation of the ferrule onto the piezo ceramic. Once the ferrule has been fixed to the piezo ceramic, two transversal cuts, one on each side of the cavity area, are made through the ferrule using a diamond wire. This procedure is undertaken in order to enhance the scan range of the cavity length, as shown in [4]. The final device can be seen in Figure 2.9.

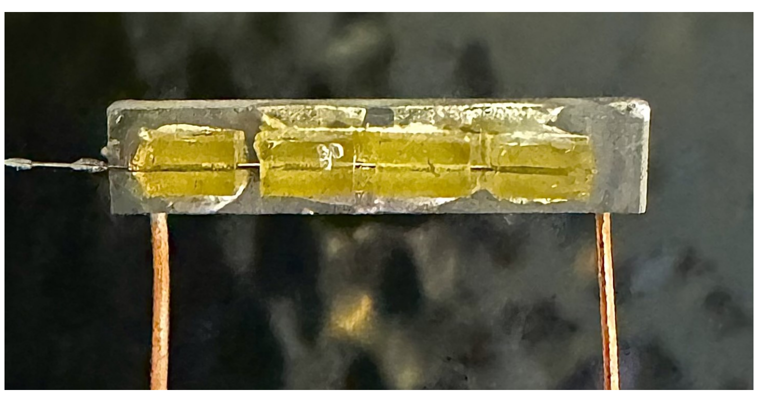

Figure 2.9: A two-channel ferrule, a piezo ceramic and two wires glued together with silver glue. Two cuts through the ferrule were sawed on each side of the cavity. Here, fibers were already inserted and fixed.

The wires need to be electrically separated through an insulator. Therefore, if silver glue happened to get onto the sides or the insulator, it needs to be scratched of, using a scalpel. A multi-meter can be used to check for short circuits between the electrical connections.
The elongation of the piezo ceramic can be calculated through [15]

$$\Delta L = \frac{d_{31} L}{H} U \tag{2.3}$$

with the piezoelectric charge coefficient $d_{31} = -210 \times 10^{-12}\,\mathrm{C\,N^{-1}}$, the length $L = 10.00(5)\,\mathrm{mm}$, the height $H = 1.00(5)\,\mathrm{mm}$ and applied voltage U.
A triangle shaped signal with a frequency of 100 Hz, with up to 786.00(8) V peak-to-peak was applied on to the piezo ceramic. This was the maximal value, which could be set with the equipment on site. This theoretically induces a length variation of the piezo ceramic of $\Delta L = 1.65(8)\,\mathrm{\mu m}$ after Equation 2.3, which is thus also the upper limit of the assembly. The consequential strain created no visible fractures on the ferrule.

2.4 Passive stability

With the wires connected to the piezo and the piezo connected to the ferrule, the coated fibers fit for usage could now be inserted.
However, instead of 1550 nm fibers which should be used for the final three-channel ferrule, 780 nm fibers were picked. This is motivated by the larger amount of sufficient 780 nm coated fibers available on-site.
Once more, due to further contraction of the polymer after being exposed to air and UV-light for a longer time period, the channel for the fibers had to be widened using a diamond wire.
With the fibers inserted into the ferrule, the distance of the fiber tips needed to be adjusted in order to achieve best possible coupling strength. For that, the fiber tip distance was scanned by moving one of the fibers with a piezo stage. The reflection signal, measured with a photo diode, was simultaneously observed with an oscilloscope. This enabled to set fiber tip distance accordingly. The obtained resonance signal is included in Figure 2.11a.

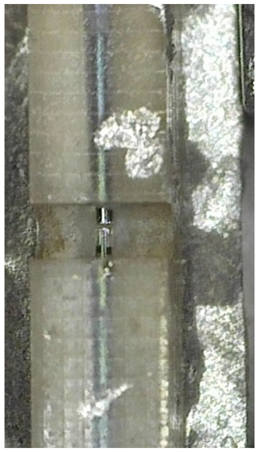

(a) Before UV-curing.

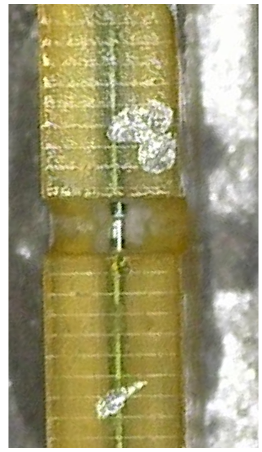

(b) After UV-curing.

Figure 2.10: Comparison of the ferrule before and after UV-curing for 1 hour.

As the fibers should be kept at the set position inside the ferrule, they needed to be permanently attached. UV glue was wiped on the channel openings, so that the glue crept into the channel. For the UV glue used, the UV curing time should be set to 1 hour. This lead to yellow staining of the polymer, see Figure 2.10. Post curing with UV-light secured the fibers, so that slightly pulling the fibers did not result in movement of the fiber tips. Nevertheless, no further contraction of the channel seemed to have taken place, as the resonance signal was still visible afterwards. Comparing the resonance signal before, see Figure 2.11a, and after securing the fibers in place, see Figure 2.11b, higher stability of the signal was reached.

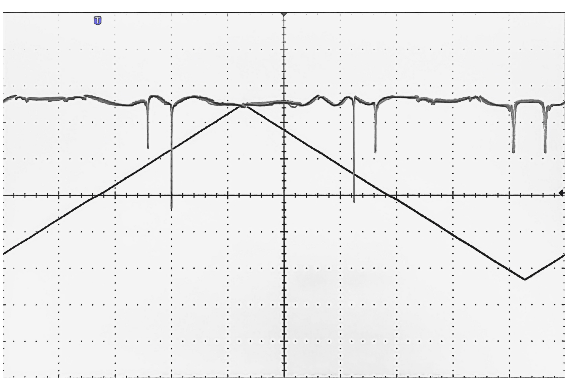

(a) Before the gluing procedure.

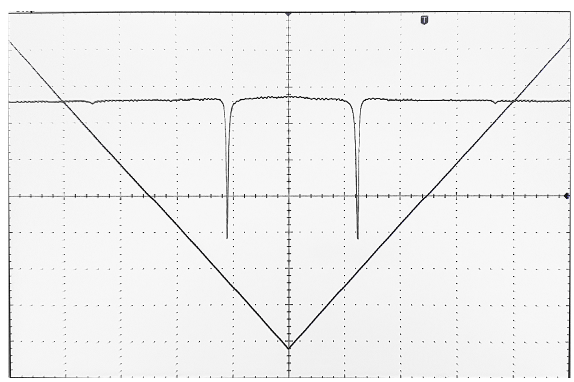

(b) After the gluing procedure.

Figure 2.11: Images of oscilloscope traces of the triangular piezo drive signal and the reflection signal of the fiber cavity. The resonance dips can be seen.

2.5 Brief summary

After finalizing the manufacturing and studying process on cavity building with a printed two-channel ferrule it can be said, that printing and developing parameters must be selected appropriately.
In particular, the contraction of the polymer cannot be neglected and needs to be addressed especially for the channel diameter. However broadening the channel with diamond wire should be avoided in order to maintain control over the actual diameter size of the channel.
The induced strain by the piezo electric effect, showed no further consequence. The original plan to scan through more than one free spectral range, given in Equation 2.2, was not possible with the electronics at hand. For that reason, the maximum range of cavity length possible with a printed ferrule could not be qualified.
Nevertheless, tuning into resonance proved to be effortlessly possible, as one can see in Figure 2.11b. The process of printing a polymer ferrule thus leads to a successfully working passively stable, tunable fiber Fabry-Perot resonator.

Chapter 3

Preparing the three-channel ferrule

With the successfully built fiber Fabry-Perot cavity with a two-channel ferrule, the manufacturing of the aimed three-channel ferrule could be approached. The discovered optimal printing parameters of the two-channel ferrule were taken into consideration when planing the design of the three-channel ferrule.

3.1 Fabrication of the three-channel ferrule

3.1.1 Design

The design of the two-channel ferrule depicted in Figure 2.8 was altered for the three-channel ferrule's design. A third extrusion, identical to each of the fiber channels for the cavity fibers, was appended orthogonal to the center of the cavity. The fibers for the pump laser, which are to be inserted into the orthogonal channel, are not coated. Hence, the diameter of the channel was set to $d_{fp} = 0.141\,\mathrm{mm}$, while the other channels feature a diameter of $d_f = 0.142\,\mathrm{mm}$. The centers of all three channels are designed in such a way, that they lie in one horizontal plane.
A groove at the cavity area, the crossing point of all three channels, was added and features curved edges. The curved edges should ease the removal of potential dirt collected inside the groove. The design is displayed in Figure 3.1.

3.1.2 Printing procedure

In light of the aforementioned findings, the printing parameters were set to:

1. Printing mode: galvo mode
2. Block splitting: 150 µm x 150 µm x 200 µm block size with a shear angle of 15°, shell and scaffold design with triangle shapes
3. Development and rinsing: 1h developing time in PGMEA, 1h rinsing time in IPA and 10 min post UV-curing in IPA

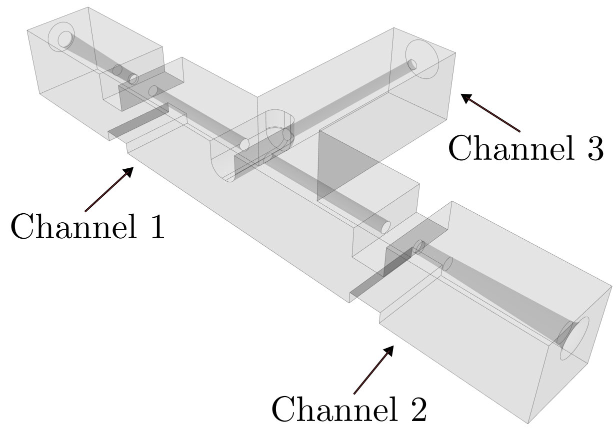

Figure 3.1: Autodesk Inventor design of a three-channel ferrule with $l = 8\,\mathrm{mm}$, $h = 1\,\mathrm{mm}$, $w = 1\,\mathrm{mm}$, the diameter of the cavity fiber channels 1 and 2 $d_f = 0.142\,\mathrm{mm}$ and its position at $h_c = 0.714\,\mathrm{mm}$, $w_c = 0.5\,\mathrm{mm}$. The extrusion of channel 3 features a length of $l_3 = 3\,\mathrm{mm}$ and a channel diameter $d_{fp} = 0.141\,\mathrm{mm}$ with all three channel center positioned in one plane. The design features additional grooves for the cavity volume and for cut-ins as well as cone-shaped channel entrances.

The block size was minimally reduced compared to the chosen block size in subsection 2.2.2. This was done as a precaution in strengthening the print and not risking any fractures during the time span of the developing and rinsing process. The printing process was completed successfully with these settings.

3.2 Piezo application

With regard to the three-channel ferrule, the intention also is to adjust the cavity length utilizing a piezo ceramic. As the connecting area between the piezo ceramic and the three-channel ferrule differs from that of the two-channel ferrule, it is necessary to re-examine the strain enforced by piezo elongation and contraction. For the three-channel ferrule to be a viable option, it is essential that the connection point of the third channel to rest of the ferrule can withstand the strain.
The piezo was attached with the same procedure and at the same position as described in section 2.3.
To assess the influence exerted by the piezo, images were captured using a 5x microscope, prior to and, using a 10x microscope, following the application of voltage to the piezo.
Since the connection point is the most fragile component of the ferrule, fractures caused by the piezo would first appear there.
Comparing the images of the connection point of the third channel before, see Figure 3.2a and after, see Figure 3.2b and Figure 3.2c, no additional fractures are visible. Consequently, the three-channel ferrule is able to sustain the tuning of the cavity length with a piezo.

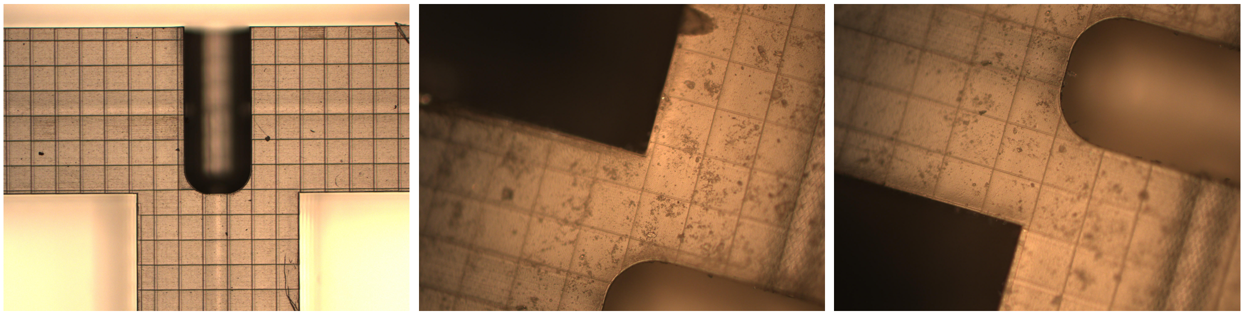

(a) 5x zoom of the connection point before tuning of the piezo length. (b) 10x zoomed left side of the connection point after tuning of the piezo length. (c) 10x zoomed right side of the connection point after tuning of the piezo length.

Figure 3.2: Microscope images of the third channel connection points before and after voltage application on the piezoceramic.

3.3 Alignment measurement

Bearing in mind that the purpose of designing a three-channel ferrule was for easing the alignment of three fiber tips to each other, a verification measurement for alignment quality was conducted. The result then provides an assessment of the precision with which the pump fiber is aligned to the cavity position inside the three-channel ferrule.

3.3.1 Concept

The transmitted intensity of a Gaussian light beam congruent to the cavity axis in the cavity region is measured, while additionally inserting a beam-blocking element in to the third channel, partially blocking the beam. As Gaussian beams are well described mathematically, an existing theoretical model can be used to compare the model to the actual measurement data. For the light beam source, a cleaved single mode 1550 nm fiber with a 0.125(5) µm fiber diameter coupled to a 1550 nm laser is inserted into one of the cavity fiber channels. Into the other cavity fiber channel a cleaved multi mode fiber coupled to a photo diode with a 0.125(5) µm fiber diameter is inserted. The multi mode fiber is able to capture the same amount of transmitted light by the single mode fiber at every possible distance inside the ferrules cavity area.
The mode of the outgoing beam of a cleaved single mode fiber tip can be modeled by a Gaussian beam [23]. The beam intensity distribution is then given by

$$I(x,y,z) = I_0 \left(\frac{w_0}{w(z)}\right)^2 \exp\left(\frac{-2(x^2+y^2)}{w(z)^2}\right) \tag{3.1}$$

with the maximum intensity I_0 and the beam waist $\omega(z)$ at a given z position. The Mode Field Diameter (MFD) defines the vertical position, where the intensity has fallen to its $I_0\,\mathrm{e}^{-2}$ value. The beam waist at origin can be sustained through $w_0 = \frac{MFD}{2}$.
With increasing distance from the fiber, the beam diverges depending on wavelength and the defined

beam properties at fiber tip position z_0. The divergence angle Θ denotes the angular extend of the beam and can be calculated for a single mode fiber through

$$\Theta = \frac{\lambda}{\pi(MFD/2)}. \tag{3.2}$$

The beam waist at distance z from the fiber tip is given by

$$w(z) = \frac{MFD}{2}\sqrt{1 + \left(\frac{z}{z_R}\right)^2} \tag{3.3}$$

with z_R defining the Rayleigh length

$$z_R = \frac{\pi}{\lambda}\left(\frac{MFD}{2}\right)^2. \tag{3.4}$$

For the single mode fiber $MFD = 6.2(3)$ µm, which was denoted by the production company [24].

Knife Edge Method

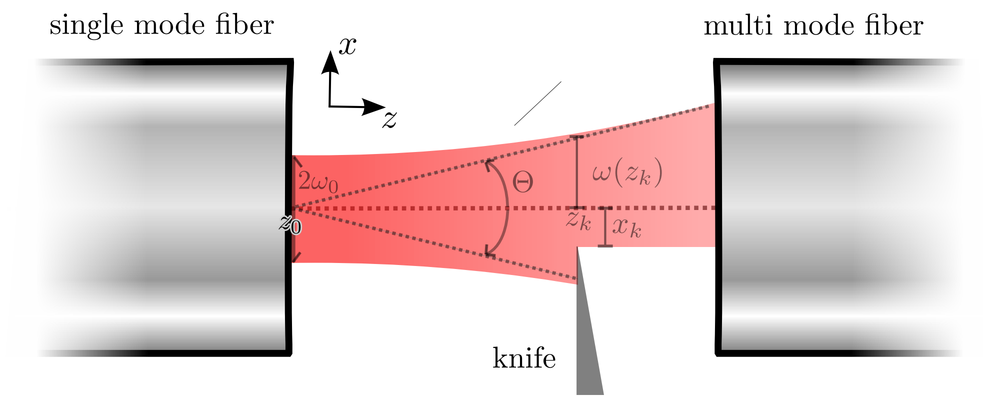

Figure 3.3: Sketch of the knife edge method. The single mode fiber position is given by z_0 and the respective beam waist ω_0 and the divergence angle Θ. The knife tip position is given by z_k and x_k and the beam waist at the knife position is given by $\omega(z_k)$.

At first idea of measuring the alignment of the fiber inserted in the third channel was to employ a typical knife edge measurement[1].

A knife is vertically inserted into the light beam. The process of measurement would entail the recording of intensity values of the transmitted light for varying penetration depths of the knife into the beam. The values should be normalized with respect to the maximum intensity measured without the knife blocking the beam propagation. A visualization of a knife edge method is depicted in Figure 3.3.

A modification to this method is to select a blocking object, which does not block the beam

[1]A thorough explanation of the knife edge method can be found in [1]

completely. This can be realized by choosing a pillar, smaller in size than the beam diameter, so that light still is transmitted on the sides of the pillar. This modification enables a position-sensitive measurement, as the transmitted beam intensity then also depends on its y-position. A visualization can be seen in Figure 3.4.

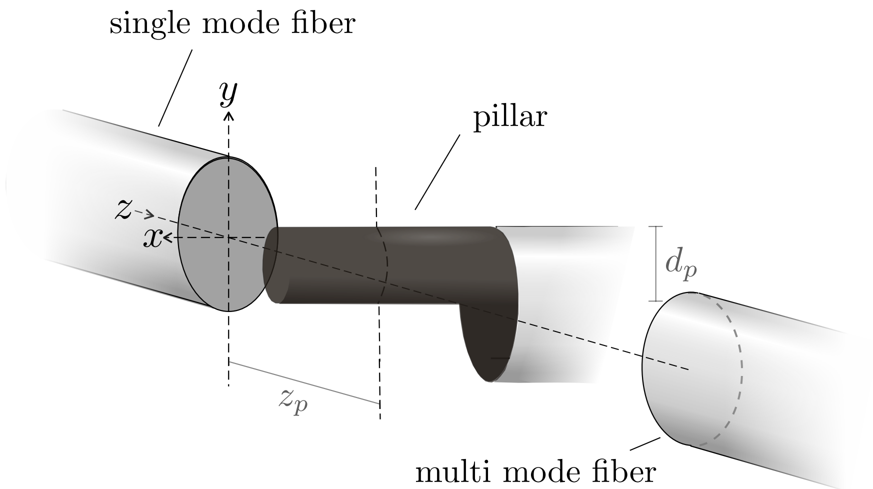

Figure 3.4: Sketch of the alignment measurement procedure inside the cavity volume of the three-channel ferrule. Laser light is emitted by a single mode fiber and captured by a multi mode fiber. A laser-pathway-blocking pillar with diameter d_p is inserted in the third channel and blocks the beam at distance z_p to the single mode fiber.

For this method, the optimal diameter size of the pillar was mathematically approximated by subtracting the transmitted intensity with complete insertion of the pillar at zero displacement and at 1 µm displacement $\Delta I = I(0\,\mu\text{m}) - I(1\,\mu\text{m})$ along the y-axis for different pillar sizes. In the approximation, the laser power $P_0 = \frac{I_0 \pi \omega_0^2}{2}$ is set to a value of 1, normalizing the integrated intensity. The z position was set to $z = 100\,\mu\text{m}$.
For a pillar diameter of $d_p = 16\,\mu\text{m}$, the deviation in intensity reaches its maximum and thus corresponds to the optimal pillar diameter with highest y-position sensitivity. This can be seen in Figure 3.5.

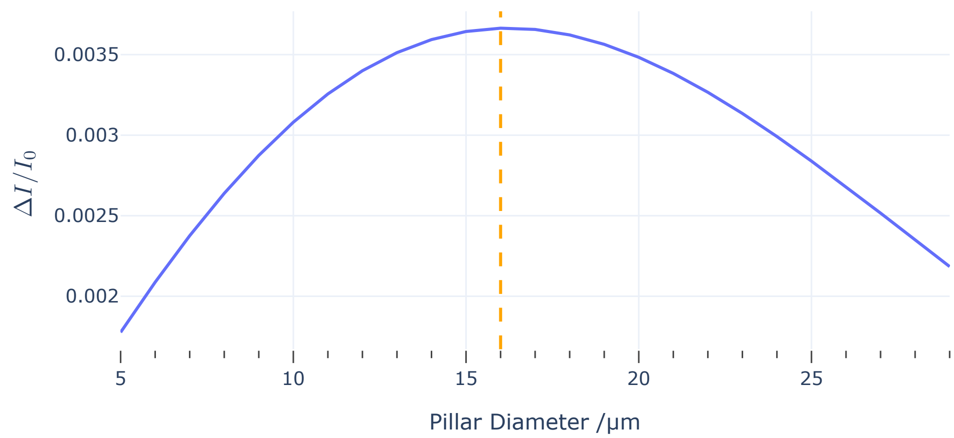

Figure 3.5: Graphical visualization of the nominated intensity deviation $\Delta I/I_0$ for different pillar diameter sizes d_p ranging from 5 µm to 29 µm. The maximal deviation is marked by a vertical orange line.

For said diameter, the intensity for different penetration depths and y-positions can be computed. The obtained intensity profiles are visualized in Figure 3.6. Nevertheless, while different approximated profiles are distinguishable in their intensity values, it might not be possible to resolve them in an actual measurement.

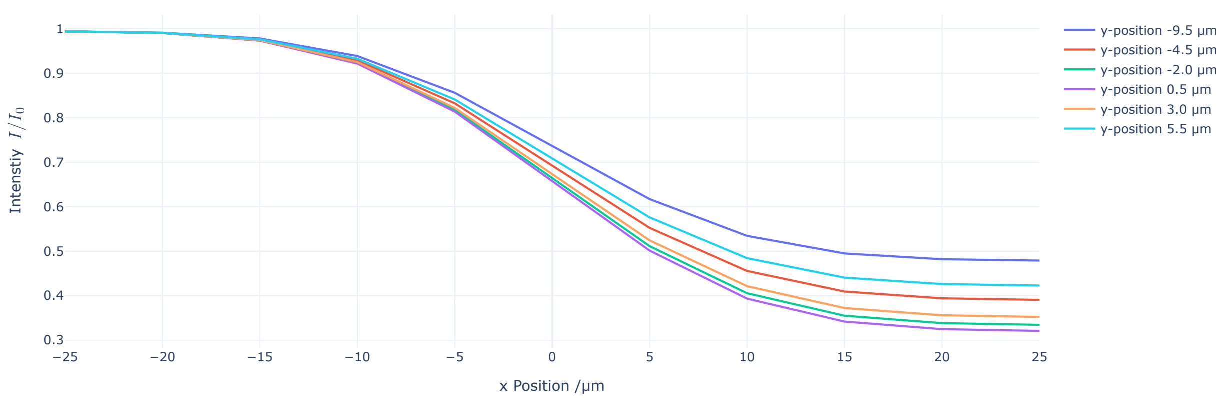

Figure 3.6: Graphical visualization of the normalized transmitted intensity I/I_0 for different penetration depths of a pillar with diameter $d_p = 16$ µm and for different y-pillar-positions.

The intensity deviation between the y-positions is at its greatest for complete penetration of the pillar through the beam. However, when considering a displacement in the y-direction of 0.5 µm, the resulting normalized intensity value for complete penetration is approximately 0.33, while a

2 µm displacement yields 0.32. Therefore, the detection device must be capable of resolving an intensity discrepancy of ∼1%. When accounting for the inherent experimental error, this is most likely not possible. Consequently, a new method that does not place such strong demands on the measurement accuracy of the technical devices is required.

180° Rotation Method

Derived from the knife edge method, approximately half of the beam is to be covered by the pillar. For that, a pillar diameter of 50 µm was chosen. The pillar is supposed to be printed on to a cleaved fiber tip. Rotating the fiber around its own axis also enables the rotation of the pillar. For the new method, two intensity values should be measured with a penetration depth, where the pillar fully blocks the beam. For the first value, the pillar should be positioned where the highest transmitted intensity is obtained. Theoretically, this is the case when the pillar is located furthest away from the center of the beam. The next value, with the pillar priory rotated by 180°, is the horizontally mirrored position in regards to the pillar mounted fiber. A sketch of the measurement positions is included in Figure 3.7.

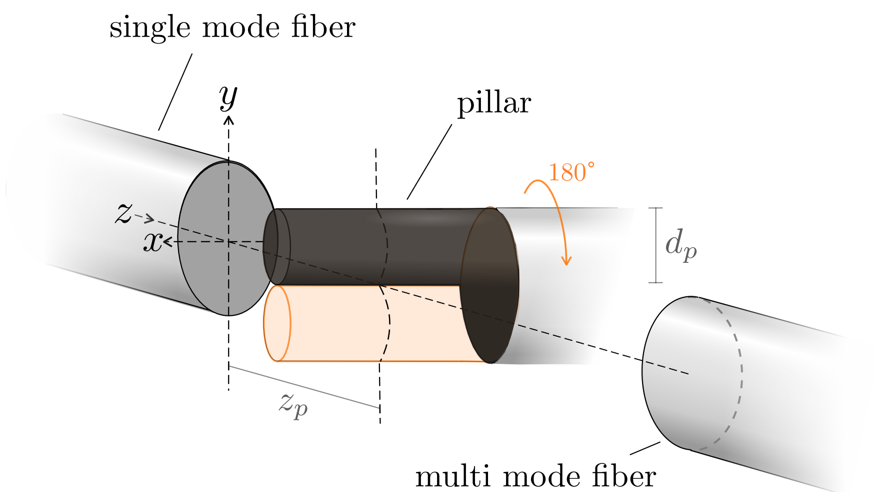

Figure 3.7: Sketch of the alignment measurement procedure inside the cavity volume of the three-channel ferrule. Laser light is emitted by a single mode fiber and captured by a multi mode fiber. A blocking pillar with diameter d_p is inserted in the third channel and blocks the beam at distance z_p to the single mode fiber. The highest intensity values, 180° apart, are to be measured.

These values then can be subtracted and assigned to the y-displacement of the pillar-mounted fiber, which then indicates the potential displacement of the channel. Under optimal conditions, both measured intensities should be of the same value, if the fibers all align in one plane.
However, another degree of freedom exists due to the uncertainty of the positioning of the pillar on the fiber end-facet, during the printing procedure.

With additional degree of freedom, another defined parameter is needed in order to determine the y-displacement of the fiber in the channel. Thus, for different y-displacements and pillar positions, not only the difference between the intensity values but also the sum is calculated.
With that, a three dimensional profile of sum and difference of intensity values and the y-displacement can be created for different positions of the pillar center in respect to the fiber tip center. This is visualized in Figure 3.8. The experimentally measured set of sum and subtraction of the intensity values can be compared with the calculated ones and their related y-position and pillar position.

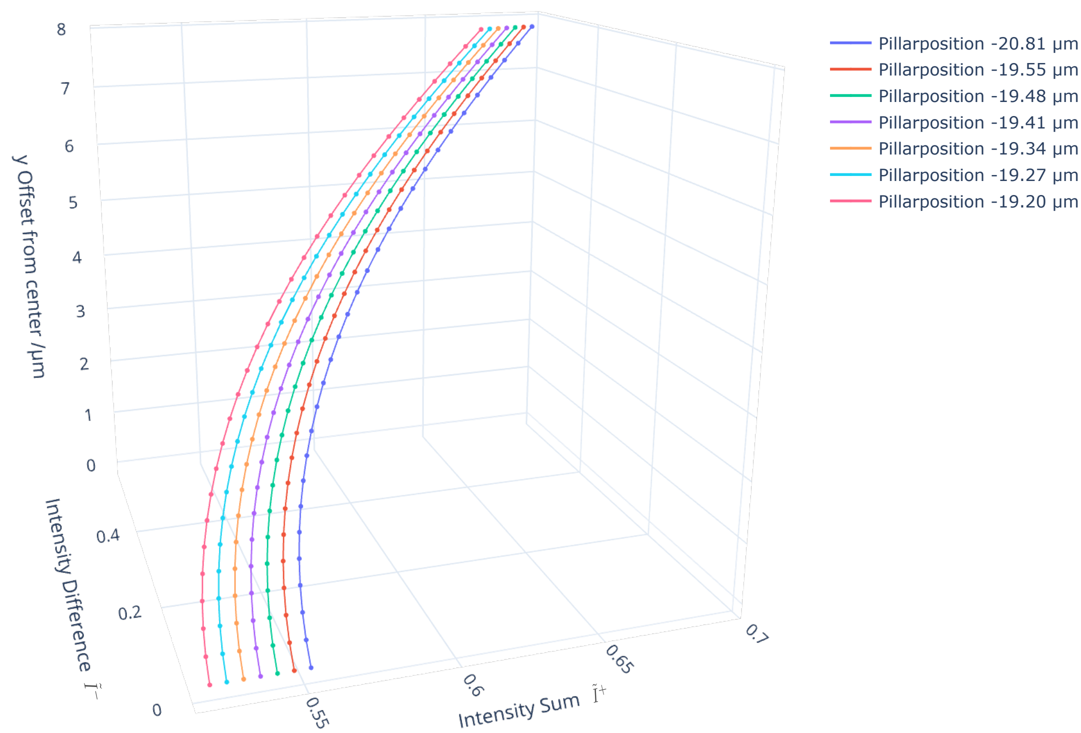

Figure 3.8: Graphical visualization of the sum and difference of the approximated normalized intensity values against the vertical y-displacement of the pillar with respect to the cavity axis for different pillar positions respectively to the pillar-mounted fiber center. The pillar diameter was set to $d_p = 50\,\mu\text{m}$ and the distance to the single mode fiber to $z_p = 100\,\mu\text{m}$.

3.3.2 Experimental execution

Pillar manufacturing

With utilization of the PPGT2, it was possible to adequately manufacture the pillar in accordance with the needed specifications. The pillar was designed as a cylindrical extension on the fiber tip, however smaller in diameter with $d_p = 50\,\mu\text{m}$. For adhesion on to the fiber tip surface, a cone-shaped transition with larger surface was added, thus, increasing the connection area of pillar and fiber. The design can be seen in Figure 3.9a.

IP-S was again used as resin. Printing settings were set to galvo mode, 20 µm x 20 µm x 20 µm block size with a shear angle of 15°.

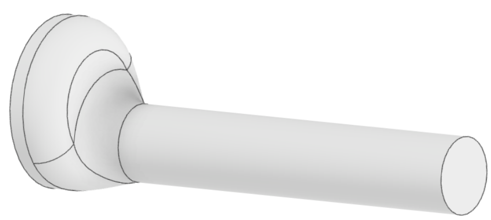

(a) Autodesk Inventor pillar design with a pillar diameter of $d_p = 50\,\mu m$, extrusion length of 3.5 mm and supporting cone diameter of 120 µm.

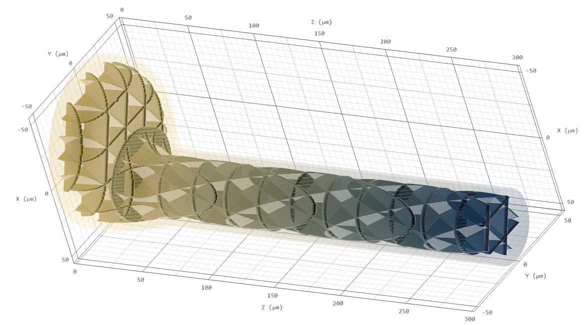

(b) Visualization of applied hexagonal lattice design for the print of the pillar.

Figure 3.9: Demonstration of the pillar design and printing lattice.

The initial selection of the triangular shell and scaffold configuration resulted in the break-off at an unknown height of the pillar extrusion during the print. For that, the scaffold shape was changed to a hexagonal shape, where the different blocks are also vertically twisted. A visualization of the lattice design is depicted in Figure 3.9b. This then enabled a successfully completed print.
Another problem during the printing process of the pillar on to the fiber tip was, that the interface could not be found automatically by the PPGT2. Therefore, this needed to be done manually utilizing the PPGT2 integrated camera. The cameras plane of focus is approximately also the plane of the lasers focus. The fiber position and surface has to be spotted and set as central as possible to the camera viewing field. Once the surface of the fiber tip has been found, the outline of the fiber tip should be set into plane of focus of the camera. A snapshot of how the surface of a cleaved fiber tip would look like in focus on the integrated camera can be seen in Figure 3. From this position, moving the focus plane into the fiber helps to ensure contact of the print and the fiber tip.

Further requirement is for the pillar to be non-transparent at the given light wavelength of 1550 nm. For the IP-S, at 1550 nm wavelength about 90% of the light is being transmitted[2]. Thus, the pillar has to be coated additionally. The simplest solution of dipping the pillar into black pigment paint was not possible as the paint also transmits at 1550 nm. Therefore, a coating with silver glue, diluted with a small amount of acetone for reducing the viscosity, was applied to the pillar. Silver has a reflection degree of $\geq 95\%$ in IR [14], and is therefore suitable as a coating material.
To inspect the impact on size of the additional coating on the pillar, microscopic images were taken before and after the application of the coating, which can be seen in Figure 3.10. With the coated pillar, see Figure 3.10b, and uncoated pillar, see Figure 3.10a, do not show any significant alteration in diameter size.

[2]The provided UV-VIS Spectrum [19] is included in Figure 4.

(a) Uncoated pillar. (b) Coated pillar with silver glue.

Figure 3.10: 5x Zoom of the pillar mounted on a fiber tip.

Intensity measurement

For the measurement, three stages were utilized. With stage 1, the cleaved single mode fiber was inserted into channel 1 and with stage 2, the cleaved multi mode fiber into channel 2. The coated pillar was inserted into the orthogonal channel 3 with stage 3, positioned on a rotating fiber holder. The holder enables a rotation range of 360°. The setup can be seen in Figure 3.11.

As further shrinkage of the channel seemed to have taken place during the month post printing, the channels needed to be broadened with a diamond wire prior to insertion.

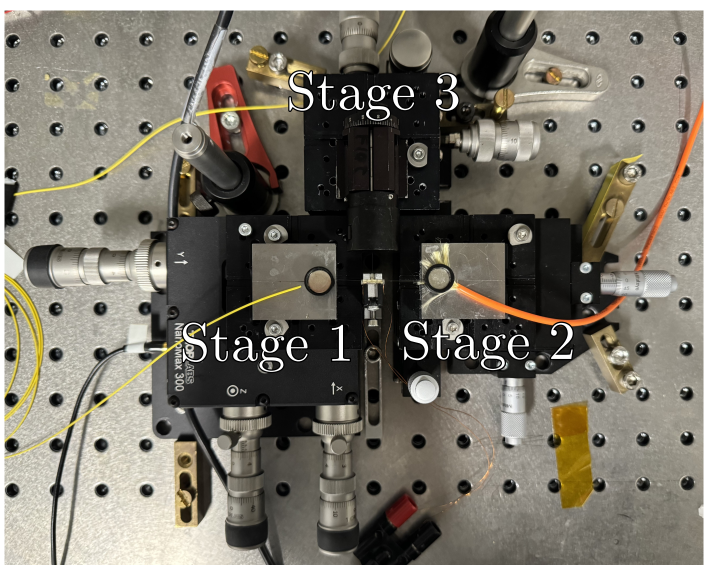

Figure 3.11: Image of the utilized setup: left stage (stage 1) with fiber holder and single mode fiber coupled to a 1550 nm laser, right stage (stage 2) with fiber holder and multi mode fiber coupled to a photo diode and top stage (stage 3) with rotating fiber holder and single mode fiber with pillar print.

The intensity value without a pillar inside was firstly recorded to $I_0 = 3400(170)\,\mathrm{mV}$. The pillar then was positioned in approximately 100(30) µm distance from the cleaved single mode fiber and inserted to such an extent that the beam along the x-axis was fully blocked. The intensity values are subsequently measured at 5° angular intervals. The pillar rotation was simultaneously monitored with an USB microscope camera, from which the rough position of the pillar can be estimated. The trend is visualised in Figure 3.12.

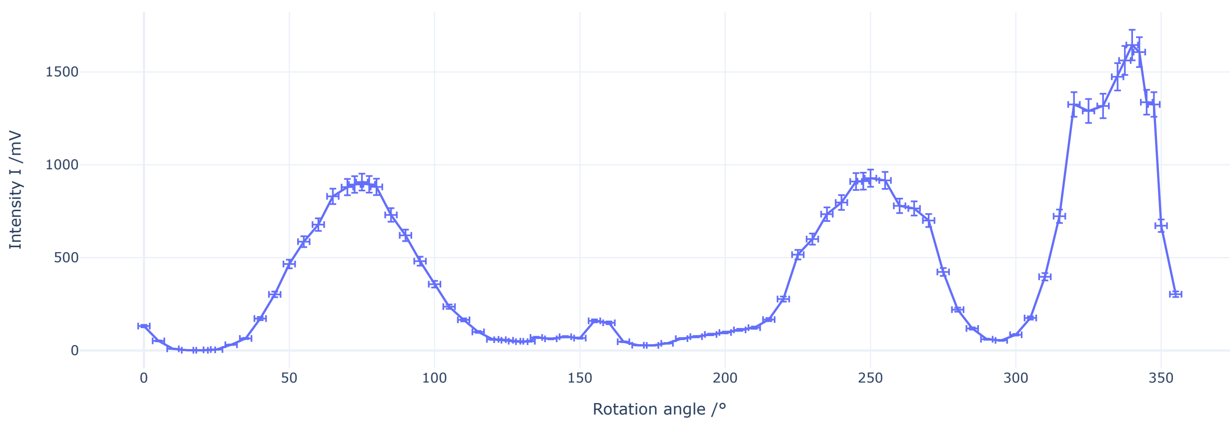

Figure 3.12: Measured intensities with the pillar intruding the laser path at 100(30) µm and 5° pillar rotation intervals. The measured intensity without the pillar was $I_0 = 3400(170)\,\mathrm{mV}$.

Coincidental verification with the camera display, the local maxima positioned in 75(5)° with $I_{75} = 907(46)\,\mathrm{mV}$ and 250(5)° with $I_{250} = 933(47)\,\mathrm{mV}$ were assigned to the highest central distance in y-direction with an estimated uncertainty of 5%. Additionally a third maximum can be seen in 340(5)° with $I_{340} = 1600(880)\,\mathrm{mV}$ intensity.

The third maximum

In order to explain the third measured maximum, a different mathematical approach was implemented, where the intensity values for the complete 360° rotation of the pillar were calculated. Further explanation of the implementation can be found in section A.1. The approximation however featured no third maximum, as can be seen in Figure 1a. This implies, that the third maximum is caused by a different process, which might be induced by the pillar coating.
The silver coating has to be heated at 120°C for 1 hour in order to completely dry. During the curing process, the semi-liquid silver glue redistributes around the printed pillar, resulting in an oval shape rather than the original cylindrical form. This can be seen in Figure 3.13.

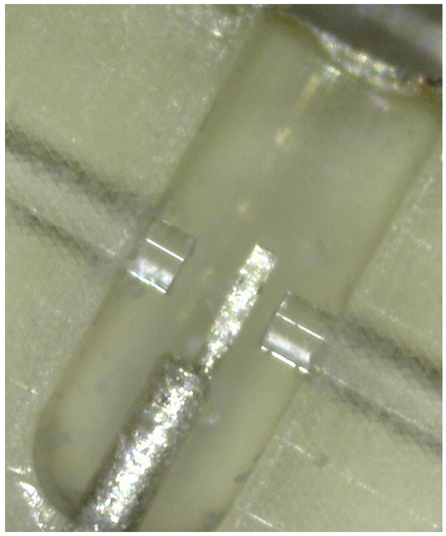

Figure 3.13: Microscope image of the silver-glue-coated pillar inside the three channel ferrule. The slightly elliptical shape of the coated pillar is visible.

As the implemented approximation demands a symmetric form of the pillar, additional effects due to a different shape are not accounted for. Also, as silver is highly reflective in the infrared, it is possible that the pillar passes through positions, where the reflected light is scattered into the multi mode fiber, thus, falsely increasing the measured intensity. $340(5)^\circ$ could correspond to such a position.
As only the intensity values to the pillars highest central distance in y-direction are needed, the third maxima was disregarded in the further evaluation of the third channel displacement.

Evaluation of the measured intensities

The identified intensity values needed for comparison to the mathematical approach depicted in Figure 3.8 can then be evaluated.
The normalized sum and difference can be sustained through

$$\tilde{I}^- = \left|\frac{I_\mathrm{i}}{I_0} - \frac{I_\mathrm{j}}{I_0}\right| \qquad\qquad \tilde{I}^+ = \left|\frac{I_\mathrm{i}}{I_0} + \frac{I_\mathrm{j}}{I_0}\right| \tag{3.5}$$

with their respective uncertainties predicted by linear error propagation theory[3].
Herewith the values were calculated to

$$\tilde{I}^- = 0.006(19) \qquad\qquad \tilde{I}^+ = 0.540(33)$$

and can be compared with the theoretical approach in Figure 3.8. With that we achieve a position of the pillars center at $-20.67(4)\,\mu\mathrm{m}$ distance from the center of the fiber and a y-direction dis-

[3]Here, calculated in python using the uncertainties package.

placement of 269(100) nm.
A displacement of 269(100) nm is well within the writing uncertainty of the PPGT2 of 1 µm [20]. With this measurement, the alignment precision of the third channel to the cavity area seems to be sufficient.
The measurement was repeated two times in one direction of rotation and one time the other way around after extracting and reinserting each fiber into their respective channel. The distance of the pillar and the single mode fiber was again set to 100(30) µm. The objective was to check for hysteresis effects. The result[4] is depicted in Figure 3.14. No significant hysteresis effects are noticeable.

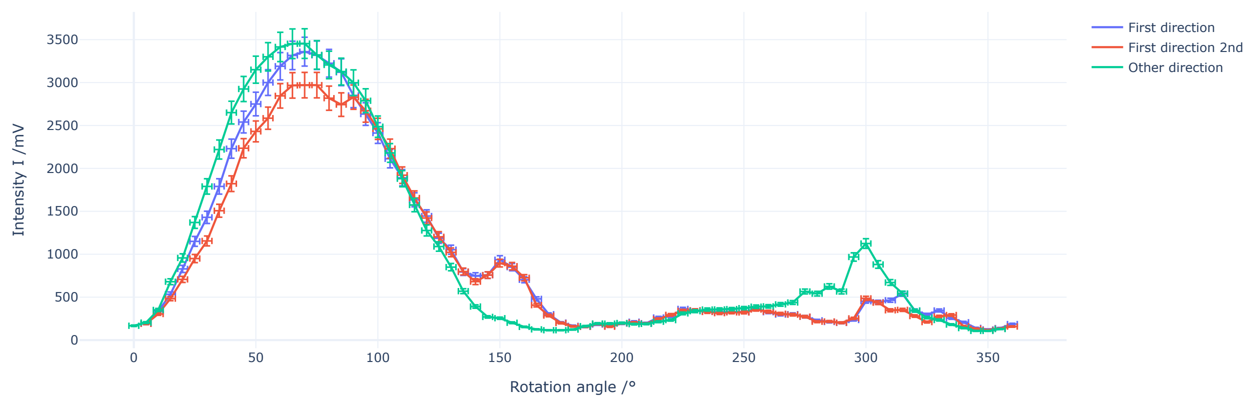

Figure 3.14: Visualization for comparison of intensity measurement with repetition two times in one direction of rotation and one time in the other. For individual representation see Figure 5

However when comparing the results of this measurement depicted in Figure 3.14 to the first measurement depicted in Figure 3.12, a dissimilar result in regards to the intensity values was obtained.
The maxima positioned at 75(5)° yields now an intensity value of a magnitude higher than the maxima positioned at 250(5)°. Again for every sequence, a maxima can be seen at 310(5)°.
For the first 360° rotation sequence, the assigned intensity values were $I_0^1 = 5663(284)\,\mathrm{mV}$ for no pillar inserted, $I_{70}^1 = 907(46)\,\mathrm{mV}$ for the local maxima positioned at 70(5)° and $I_{250}^1 = 933(47)\,\mathrm{mV}$ for 250(5)° resulting in

$$\tilde{I}_1^- = 0.52(4) \qquad \tilde{I}_1^+ = 0.66(4)$$

For the second measurement sequence in the same direction of rotation, the assigned intensity values were $I_0^1 = 5663(284)\,\mathrm{mV}$, $I_{70}^1 = 3025(152)\,\mathrm{mV}$ for 70(5)° and $I_{250}^1 = 388(20)\,\mathrm{mV}$ for 250(5)°

[4]Here, only the plot with every measurement combined is inserted. For individual visualization see Figure 5

resulting in

$$\tilde{I}_2^- = 0.47(4) \qquad \tilde{I}_2^+ = 0.60(4)$$

For the third measurement sequence in the other direction of rotation, intensity values were $I_0^1 = 5698(285)\,\text{mV}$, $I_{70}^1 = 3463(173)\,\text{mV}$ for $70(5)^\circ$ and $I_{250}^1 = 361(19)\,\text{mV}$ for $250(5)^\circ$ resulting in

$$\tilde{I}_{-1}^- = 0.54(4) \qquad \tilde{I}_{-1}^+ = 0.67(5)$$

For comparing the result with the mathematical approach, the mean values and the associated uncertainties, given by linear error propagation theory of the three measurements

$$\bar{I}^- = 0.510(23) \qquad \bar{I}^+ = 0.643(25)$$

were chosen. With that, the pillars center position was determined to be at $-20.32(4)\,\mu\text{m}$ displacement from the center of the fiber and a $7.0(1)\,\mu\text{m}$ y-direction offset of the third channel. This value implies a displacement in y-direction higher in magnitude than the priory obtained value from the first measurement.

This can be reasoned by the re-adjustment of the fibers. Observing the fibers with the USB microscope camera, one could see, that the fibers were able to move in large amounts inside the channels. From that it can be concluded, that post broadening with a diamond wire should be avoided if aiming to build a stable cavity. The procedure is inaccurate and can not be controlled sufficiently, which might have lead to an oversized and unevenly surfaced channel, with which displacement in unpredictable amounts is possible.

For the first measurement, positions of the fibers inside the respective channels supposedly lead to better alignment.

The overall results predict an insufficient alignment for the intended use of photothermal gas detection as of yet.

Chapter 4

Conclusion and Outlook

The aim of this thesis was to manufacture a three-channel ferrule fit for photothermal gas detection. For this, the first step was to find fiber mirrors suitable for building a tunable fiber Fabry-Perot cavity with a probe laser wavelength of 1550 nm. As the yield of suitable fiber mirrors for a laser wavelength of 1550 nm was relatively low, processes of elimination were applied prior to properly testing the fiber mirrors for resonances. This sped up the searching process so that two fiber mirrors with a coupling depths of 30% and 60% were found.
The second step was to understand the working principles of 3D printing with the PPGT2 and how those would affect the ferrule's properties. Starting the printing procedures, a two-channel ferrule was fabricated. Especially the observed degree of shrinkage of the printed ferrule's channel diameter stood out. This needs to be accounted for when choosing the size of the channel's diameter. As shrinkage can still happen one month post printing, methods to expedite the shrinking process should be thought of. Ideas are to expose the ferrule to heat or to a vacuum environment for longer time periods. This should sped up the shrinking process.
Applying strain with a piezoelectric element as well as inserting and fixating fibers into the channels resulted in no further problems. With that it was possible to successfully build a monolithic, passively stable and tunable fiber Fabry-Perot cavity using a printed ferrule.
Next, the third step of printing a three-channel ferrule was carried out. Again applying strain with a piezo electric element resulted in no further issues.
As photothermal gas detection demands a precise positioning of the pump fiber relative to the cavity area, an alignment measurement for the third channel was performed. Inspired by the knife edge method, a modified approach was carried out, where higher sensitivity could be reached. For this purpose, a mathematical model was implemented to which the actual measurement was compared. Repetition of the measurement led to dissimilar results of a displacement from 269(100) nm up to 7.0(1) µm of the overall positioning of the fiber inserted into the third channel. This can be explained by the hard to control broadening procedure with a diamond wire of the channels and should be avoided.
For future prospects, it is mandatory to further pursue the optimization of the channel diameter of printed ferrules. When this is accomplished, the alignment measurement should be carried out

again and the monolithic, passively stable and tunable fiber Fabry-Perot cavity for photothermal gas detection can then be further pursued.

To further improve the system, a multi mode fiber could be permanently fixaded into the third channel as the pump fiber. This would enable gas detection of various analytes without the need to exchange the pump fiber in order to adapt to the wavelength of the pump laser.

Another prospect would be not only detecting gas but also liquids with the finished device, which could open up an even broader range of applications. However, for that the strong thermal response of liquids needs to be accounted for.

Finally, even though the envisioned monolithic, passively stable and tunable fiber Fabry-Perot cavity for photothermal gas detection could not be manufactured as of yet, promising results were obtained and printing a three-channel ferrule should be further pursued.

Bibliography

[1] Marcos Araújo et al. "Measurement of Gaussian laser beam radius using the knife-edge technique: Improvement on data analysis". In: *Applied optics* 48 (Feb. 2009), pp. 393–396. DOI: 10.1364/AO.48.000393.

[2] W. Demtröder. *Experimentalphysik 2: Elektrizität und Optik*. Springer-Lehrbuch. Springer Berlin Heidelberg, 2018, pp. 194–208. ISBN: 9783662557907.

[3] Julia Purtov et al. "Improved development procedure to enhance the stability of microstructures created by two-photon polymerization". In: *Microelectronic Engineering* 194 (2018), pp. 45–50. ISSN: 0167-9317. DOI: https://doi.org/10.1016/j.mee.2018.03.009. URL: https://www.sciencedirect.com/science/article/pii/S0167931718301205.

[4] Carlos Saavedra et al. "Tunable fiber Fabry-Perot cavities with high passive stability". In: *Optics Express* 29.2 (Jan. 2021), p. 974. ISSN: 1094-4087. DOI: 10.1364/oe.412273. URL: http://dx.doi.org/10.1364/OE.412273.

[5] Lukas Tenbrake. "Fiber Cavity Optomechanics with Polymer Membranes". MA thesis. Friedrich-Wilhelms University, 2021.

[6] H. Pfeifer et al. "Achievements and perspectives of optical fiber Fabry–Perot cavities". In: *Applied Physics B* 128.2 (Jan. 2022). ISSN: 1432-0649. DOI: 10.1007/s00340-022-07752-8. URL: http://dx.doi.org/10.1007/s00340-022-07752-8.

[7] Pooja Saxena and Prashant Shukla. "A Review on Gas Sensor Technology and Its Applications". In: *Computational and Experimental Methods in Mechanical Engineering*. Ed. by Veeredhi Vasudeva Rao et al. Singapore: Springer Singapore, 2022, pp. 165–175. ISBN: 978-981-16-2857-3.

[8] Alexander Faßbender. "Adding New Functionalities to Optical Fiber Cavities by Direct Laser Writing". PhD thesis. Rheinische Friedrich-Wilhelms-Universität Bonn, Dec. 2023. URL: https://hdl.handle.net/20.500.11811/11177.

[9] Karol Krzempek et al. *Photothermal gas detection using a miniaturized fiber Fabry-Perot cavity*. 2023. arXiv: 2311.12536 [physics.optics]. URL: https://arxiv.org/abs/2311.12536.

[10] Meenakshi Singh and Ritu Singh. “Chapter 1 - An introduction to molecularly imprinted polymers”. In: *Molecularly Imprinted Polymers (MIPs)*. Ed. by Meenakshi Singh. Elsevier, 2023, pp. 1–48. ISBN: 978-0-323-91925-8. DOI: https://doi.org/10.1016/B978-0-323-91925-8.00012-0. URL: https://www.sciencedirect.com/science/article/pii/B9780323919258000120.

[11] Rytis Mitkus. “Piezoelectricity and Piezoelectric Materials”. In: *Ultraviolet Light Curable Piezoelectric Multi-phase Composites*. Cham: Springer Nature Switzerland, 2024, pp. 15–50. ISBN: 978-3-031-56946-3. DOI: 10.1007/978-3-031-56946-3_3. URL: https://doi.org/10.1007/978-3-031-56946-3_3.

[12] EPFL. *Describe Manual*. URL: https://www.epfl.ch/research/facilities/cmi/equipment/photolithography/nanoscribe-photonic-professional-gt/describe-manual/ (visited on 08/01/2024).

[13] LAYERTEC GmbH. *LAYERTEC - Your supplier for enhanced laser optics*. URL: https://www.layertec.de/de/ (visited on 07/25/2024).

[14] LAYERTEC GmbH. *metallische Beschichtungen*. URL: https://www.layertec.de/de/capabilities/coatings/metallic/ (visited on 07/25/2024).

[15] PI Ceramic GmbH. *Piezokeramik Platten und Blöcke*. URL: https://www.piceramic.de/de/produkte/piezokeramische-komponenten/platten-und-bloecke (visited on 07/19/2024).

[16] © 2024 Autodesk Inc. *Autodesk Inventor: 3D modeling software for designers and engineers*. URL: https://www.autodesk.com/asean/products/inventor/overview?term=1-YEAR&tab=subscription (visited on 08/01/2024).

[17] © 2007-2024 Nanoscribe GmbH Co. KG. *Photonic Professional GT2*. URL: https://www.nanoscribe.com/en/products/photonic-professional-gt2/#tab-15516 (visited on 08/01/2024).

[18] Diamond WireTec GmbH Co. KG. *Diamond wires on spool*. URL: https://www.diamondwiretec.com/diamond-wires/diamond-wires-on-spool.html (visited on 07/20/2024).

[19] Nanoscribe. *IP-S*. URL: https://support.nanoscribe.com/hc/en-gb/articles/360001750353-IP-S (visited on 07/18/2024).

[20] Nanoscribe. *Nanoguide*. URL: https://support.nanoscribe.com/hc/en-gb/categories/360000826253-General-Information (visited on 07/18/2024).

[21] Nanoscribe. *Printing Modes*. URL: https://support.nanoscribe.com/hc/en-gb/articles/214082985-Printing-Modes#Ch:PPGT (visited on 07/18/2024).

[22] Nanoscribe. *Structural Deformation*. URL: https://support.nanoscribe.com/hc/en-gb/articles/360002381814-Structural-Deformation (visited on 07/20/2024).

[23] Inc. Thorlabs. *Insights into Fiber Optics*. URL: https://www.thorlabs.com/newgrouppage9.cfm?objectgroup_id=12211 (visited on 06/01/2024).

[24] Inc. Thorlabs. *Single Mode FC/APC Fiber Optic Patch Cables*. URL: https://www.thorlabs.com/newgrouppage9.cfm?objectgroup_id=334&pn=P3-1064Y-FC-5 (visited on 07/03/2024).

Appendix

A.1 Numerical implementation of the 360° rotation

In order to explain the maxima at 310°, a model not only for two positions of the pillar, but instead for the complete 360° rotation sequence has been implemented.
To recreate the rotation, the projection on the x-y plane through the pillars center were calculated. The beam intensity of the planes position and the pillars y-position can be calculated through

$$h_i = R \sin\theta_i \qquad \omega_i = \frac{MFD}{2}\sqrt{1+\left(\frac{z_0 + R\cos\theta_i}{z_R}\right)^2} \tag{1}$$

with R being the radius of the rotation of the pillar in regard to the pillars center and the pillar-mounted fiber. With that for every $\theta_i = \theta_{i-1} + 5°$ the intensity can be approximated and compared to the measured value.
Based on the result from the former implemented approximation, the pillar position on the fiber tip was assumed to be at $-20.32(4)$ µm displacement from the center of the fiber. For the displacement in y-direction, optimal alignment and a misalignment of 7 µm as evaluated in section 3.3.2. The results can be seen in Figure 1a for optimal alignment and Figure 1b for 7 µm misalignment.

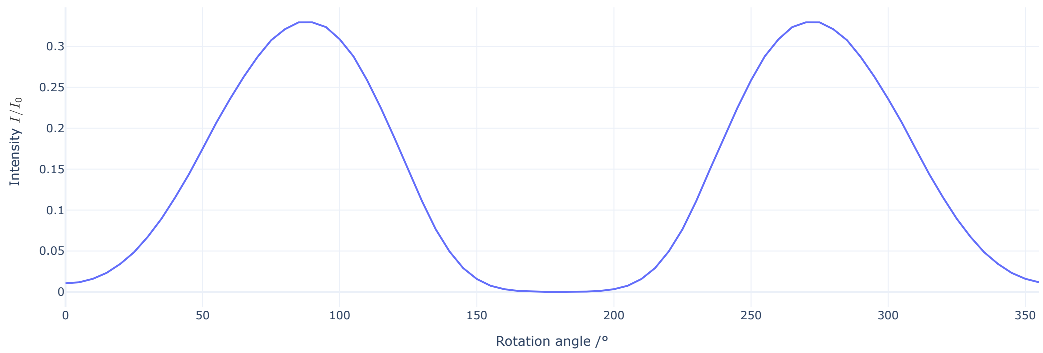

(a) Normalized intensity profile for 0 µm misalignment of third channel.

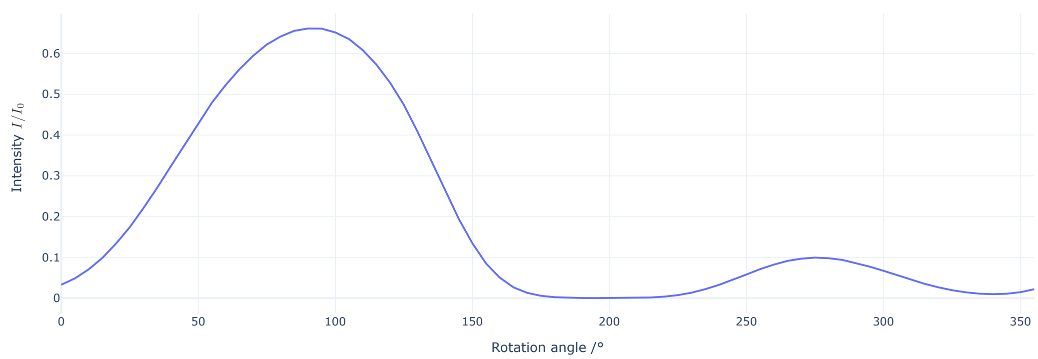

(b) Normalized intensity profile for 7 µm misalignment of third channel.

Figure 1: Implemented profiles for 5° rotation intervals with set distance 100 µm between center of pillar-mounted fiber and single mode fiber, a pillar diameter of 50 µm and a pillar position on the fiber of −20.32 µm.

Comparing the calculations more accurately with the measured sequences, the intensity values of the first measurement sequence, depicted in Figure 3.12 and the measurement sequence depicted in Figure 5c were normalized with their respective I_0 values and plotted together, which can be seen in Figure 2.
It can be said, that the implemented profiles roughly match the intensity values.

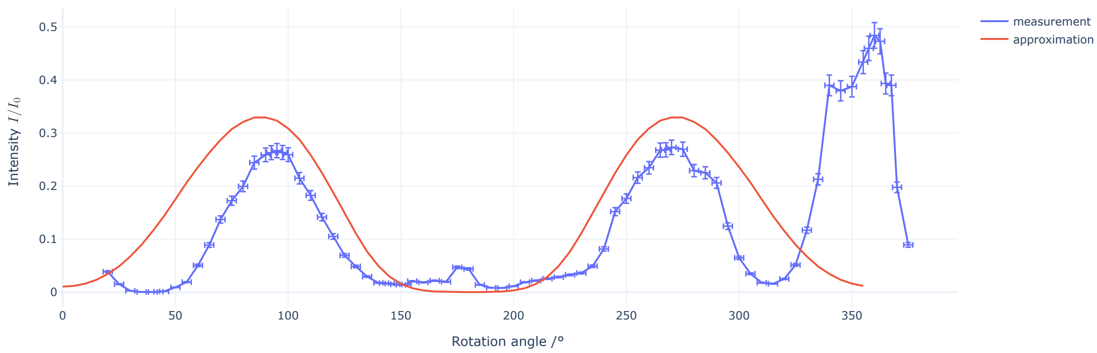

(a) Measurement sequence depicted in Figure 3.12 with implemented sequence depicted in Figure 1a.

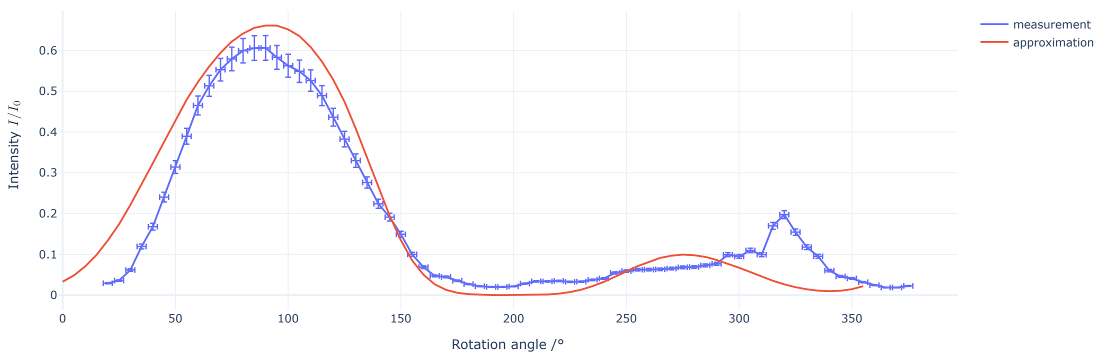

(b) Measurement sequence depicted in Figure 5c with implemented sequence depicted in Figure 1b.

Figure 2: Normalized measured values plotted together with the implemented normalized values.

B.1 Additional images

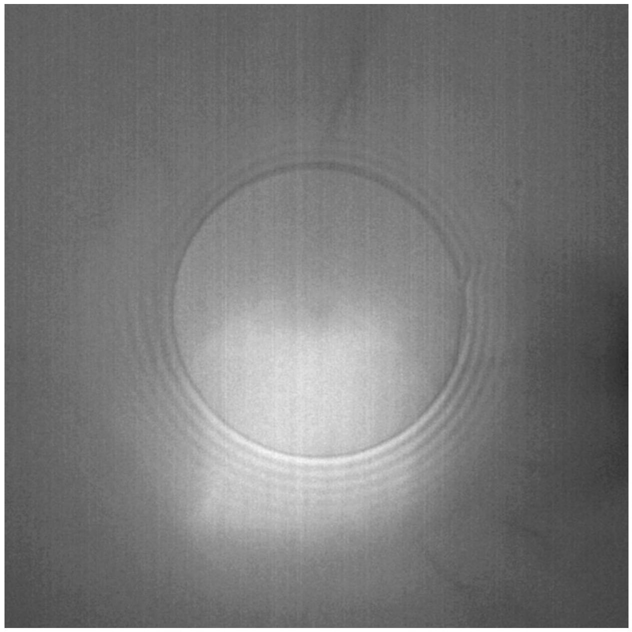

Figure 3: Image of cleaved fiber tip with the fiber tip in focus of the integrated camera of the PPGT2.

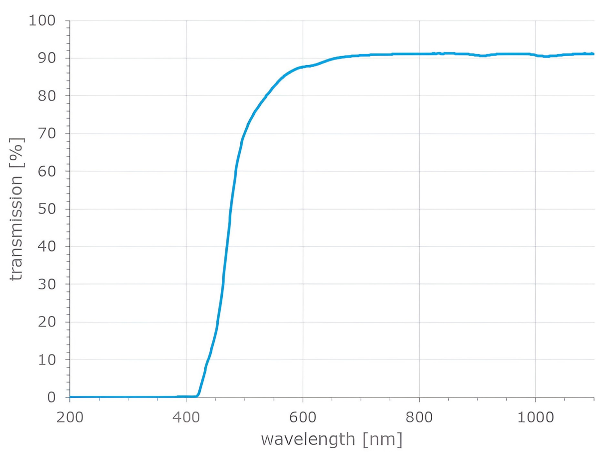

Figure 4: UV-VIS Spectrum (transmission through 0.981 mm thick, 1PP/UV-cured sample)[19]

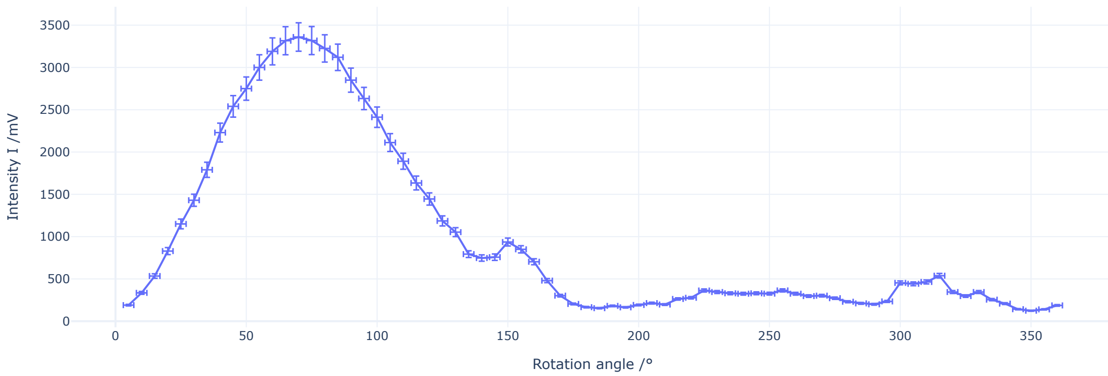

(a) Measurement sequence with rotation in decreasing angle direction. The measured intensity without the pillar was $I_0 = 5663(284)\,\mathrm{mV}$.

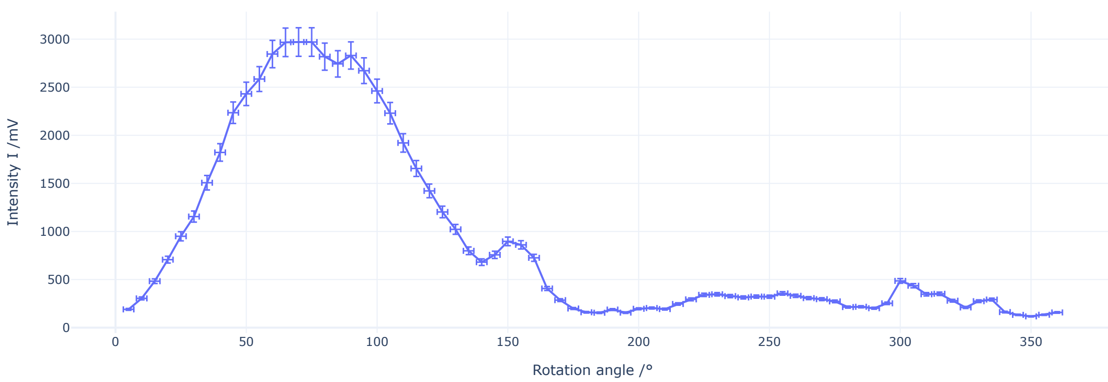

(b) Second measurement sequence with rotation in decreasing angle direction. The measured intensity without the pillar was $I_0 = 5663(284)\,\mathrm{mV}$.

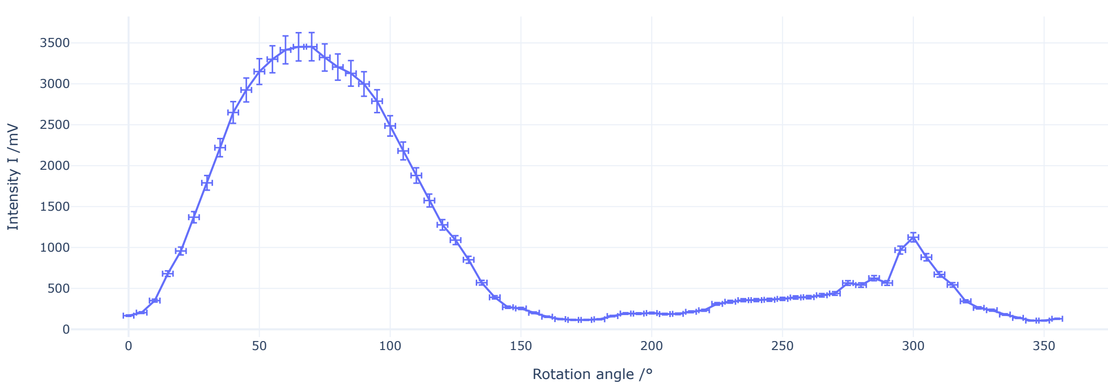

(c) Measurement sequence with rotation in increasing angle direction. The measured intensity without the pillar was $I_0 = 5698(285)\,\mathrm{mV}$.

Figure 5: Measured intensities $100(30)\,\mu\mathrm{m}$ distance between pillar and single mode fiber and 5° pillar-rotation intervals.